*R*esearch in
*A*stronomy and
*A*strophysics

A survey of CO and its isotope lines for possible cloud-cloud collision candidates

Nan Li and Jun-Jie Wang

National Astronomical Observatories, Chinese Academy of Sciences, Beijing 100012, China; *linan@bao.ac.cn*

Abstract In the ^{12}CO (J=1–0) survey of 1331 cold *IRAS* sources, 214 sources show profiles with multiple peaks and are selected as cloud-cloud collision candidates. In January 2005, 201 sources were detected with ^{12}CO(1–0), ^{13}CO(1–0), and C^{18}O(1–0) emissions by the 13.7 m telescope at Purple Mount Observatory. This is the first survey of CO and its isotope lines directed toward possible cloud-cloud collision regions. According to the statistics of the 201 sources in the Galactic distribution, the 201 sources show a similar distribution to the parent sample (1331 cold *IRAS* sources). These sources are located over a wide range of Galactocentric distances, and are partly associated with the star forming region. Based on preliminary criteria which describe the spectral properties of the possible cloud-cloud collision region, the 201 sources are classified into four types by the fit of the spectral profiles between the optically thick and thin lines toward each source. The survey is focused on possible cloud-cloud collision regions, and gives some evidence to help us with selecting the target region. We will continue the process of mapping and studying multi-wavelength observations for the selected region in the future.

Key words: stars: formation — ISM: clouds — ISM: molecules

1 INTRODUCTION

In star forming regions, a collapse could be triggered by self-gravitation or some external interaction mechanisms. Besides other external shocks (e.g. supernova shocks, stellar winds around a previous generation of OB stars, etc.), a cloud-cloud collision was also proposed as an effective external mechanism influencing star formation. These processes have been calculated with numerical simulations (Hausman 1981; Gilden 1984; Lattanzio et al. 1985; Habe & Ohta 1992). When CO and its isotope molecules are used by astronomers as a sensitive probe to detect cool molecular regions, many CO surveys can be conducted to describe the distributions of molecular clouds (Goldreich & Kwan 1974; Frerking & Langer 1982). For a region showing cloud-cloud collision, CO and its isotope lines are also good probes to describe the cloud collision region (Wang et al. 2004; Xin & Wang 2008). The *IRAS* point-source database is an effective indicator of the star forming regions which are hidden by dust in visible wavelengths. In this paper, we choose the cold *IRAS* source according to our criteria to survey CO and its isotope lines. This is a relatively complete *IRAS*-based CO survey for possible cloud-cloud collision candidates. Although some observations were done in earlier times (Kerton & Brunt 2003), they only covered a small part (42 sources) of our sample in the ^{12}CO line. There

are no previous results with ^{12}CO(1–0), ^{13}CO(1–0), or C^{18}O(1–0) emissions for possible cloud-cloud collision candidates. We have selected two possible cloud-cloud collision candidates (IRAS 02459+6029 and 22528+5936) from our survey which observed ^{12}CO(2–1), ^{13}CO(2–1), ^{12}CO(3–2), and ^{13}CO(3–2) by KOSMA in previous work (Li & Wang 2012). The CO mapping and multi-wavelength study show that IRAS 02459+6029 could be an example of cloud-cloud collision and IRAS 22528+5936 could be two separate clouds that are not colliding.

2 SAMPLE SELECTION

We build the sample list on the basis of the ^{12}CO(1–0) survey of the cold *IRAS* sources (Yang et al. 2002). These 1331 sources were selected from the cold *IRAS* sources according to the following criteria:

(1) (a) α(B1950) $\leq$ 8$^\mathrm{h}$, α(B1950) $\geq$ 16$^\mathrm{h}$, δ(B1950) $\geq$ $-35°$; (b) $|b| \leq 25°$; or (c) $|b| \geq 1°$ when $l \leq 60°$ or $l \geq 300°$. Coordinates of sources should obey the conditions. (a) and (b) cover the sources in the northern sky near the Galactic plane and avoid confusing CO in the source from that in the Galactic central region.
(2) Sources should be detected in at least three wave bands to specify their infrared properties.
(3) Source colors over the 12, 25, and 60 μm bands should satisfy log(F12/ F25) $\leq$ -0.4 and log(F25/ F60) $\leq$ -0.4 or log(F12/ F60) $\leq$ -0.4 when the FQUAL25 = 1. These cold *IRAS* color ranges are derived from statistical data for the embedded sources associated with recent star formation (Beichman 1986).
(4) These sources are not associated with late-type stars, planetary nebulae, extra galaxies, or other kinds of sources unrelated with Galactic star formation identified by the *IRAS* Point Source Catalog (PSC).

We then selected our sample list based on the criteria for possible cloud-cloud collision candidates from 1331 cold *IRAS* sources. According to a set of criteria given by Vallee (1995a) which describe the spectral properties of the possible cloud-cloud collision region, we choose the samples for which the line profile shows double or multiple peaks and the location of peaks is sequential. It means that this kind of source may have several velocity components and it might include several colliding cloud clumps. Figure 1 shows the CO(1–0) spectrum that we selected from the 1331 cold *IRAS* sources.

After this step, there were 214 sources that were selected. However, only 201 sources were detected in the ^{12}CO(1–0), ^{13}CO(1–0), and C^{18}O(1–0) lines. The galactic distribution of the 201 sources is displayed in Figure 2. Most of the sources are located around the Galactic plane. Some of the sources are concentrated toward the well-known local star-forming regions, particularly toward the Perseus, Taurus, and Orion regions at $l = 160°$ to $200°$ and $b = -10°$ to $-25°$.

3 OBSERVATIONS

These sources were already observed in ^{12}CO(1–0), ^{13}CO(1–0) and C^{18}O(1–0) with the 13.7 m (45 foot) Millimeter Telescope at Qinghai Station of Purple Mountain Observatory, CAS (Chinese Academy of Sciences), in January 2005. The beam size was 50±7 arcsec in azimuth and 54±3 arcsec in elevation. The pointing accuracy was around 5 arcsec. We used the cooled mixer SIS receiver which has three acousto-optical spectrometers (AOSs) working at 110.20, 109.78 and 115.27 GHz to simultaneously acquire the three respective CO(1–0) lines. The AOS had 1024 channels, and its band widths for ^{12}CO(1–0),^{13}CO(1–0) and C^{18}O(1–0) lines were 145.330, 42.672 and 43.097 MHz respectively. The system temperature was 200–300 K during observations. The noise level of the antenna's temperature was typically 0.4 K for ^{12}CO(1–0), 0.3 K for ^{13}CO(1–0) and 0.2 K for C^{18}O(1–0). In this paper, we do not apply main-beam efficiency corrections to any data, but rather simply show the data in the original antenna temperature scale T_A^*.
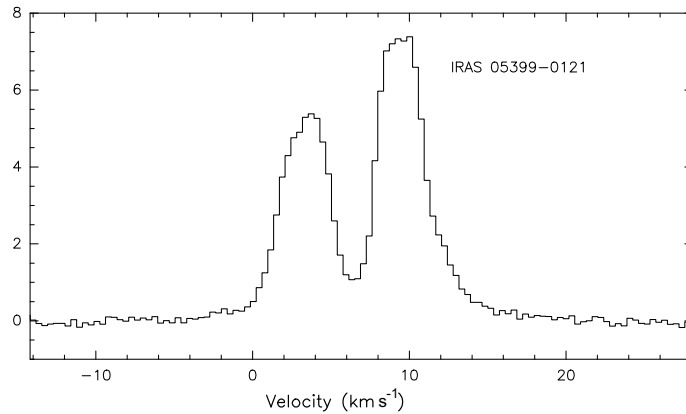
Fig. 1 The $^{12}CO(1–0)$ line profile of a sample initially selected for a possible cloud-cloud collision from 1331 *IRAS* sources (Yang et al. 2002).
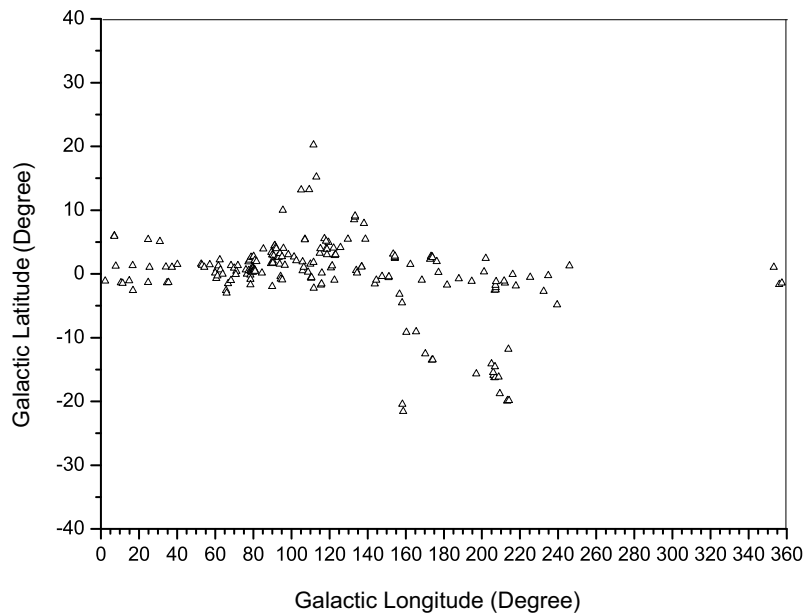
Fig. 2 Galactic distribution of the 201 sources which are selected as cloud-cloud collision candidates.

We observed these sources in position-switching mode in order to obtain a better baseline. Each source was scanned at least two times except for a few sources that were measured many times due to bad signal to noise ratio (SNR). The integration time was two minutes on every source. We identified a source to be detected if its peak antenna temperature was larger than the 3σ rms noise level. We observed the standard sources, such as W51D, S140, W3(OH), NGC 2264, etc., every two hours during the observation. These standard sources served as the secondary temperature standard. We used them to calibrate target sources within a specific period of time for reducing the influence of any possible short-period variation of the system.

The data reduction was based on the software packages CLASS (Continuum and Line Analysis Single-dish Software) and GREG (Grenoble Graphic).

4 RESULTS

4.1 The Statistical Study of the Selected CO Sources

The 201 sources are observed in ^{12}CO(1–0), ^{13}CO(1–0) and C^{18}O(1–0).

Table 1 shows the basic parameters of 201 sources as possible cloud-cloud collision candidates. Column (1) shows the *IRAS* name of the sources, and Cols. (2) and (3) denote equatorial coordinates in the J2000 epoch. Columns (4) and (5) are their Galactic coordinates, and Col. (6) shows the peak temperature of the antenna on each source. Column (7) is the corresponding rms noise level of the CO spectrum, and Col. (8) contains the radial velocity of the sources relative to the local standard of rest. In Col. (9), the FWHM of each line derived from a Gaussian fitting is presented. Column (10) lists the line span measured at the 0 K level, while Col. (11) gives the kinematic distance of each source which is derived from Yang et al. (2002).

Table 1 Basic parameters of the 201 selected *IRAS* sources. In this table, 42 sources, denoted with an asterisk, were also observed by the FCRAO Outer Galaxy Survey (Kerton & Brunt 2003).

Name	α(2000) (h m s)	β(2000) (° ′ ″)	l (°)	b (°)	T_A^* (K)	T_σ (K)	V_{LSR} (km s^{-1})	δV (km s^{-1})	V_{span} (km s^{-1})	D_k (kpc)
(1)	(2)	(3)	(4)	(5)	(6)	(7)	(8)	(9)	(10)	(11)
*00021+6604	00 04 43.60	+66 20 58.0	118.26373	3.901982	2.53	0.15	−7.53	2.94	5.65	0.45
*00056+6605	00 08 18.80	+66 21 53.0	118.621328	3.854562	2.89	0.12	−14.34	1.47	3.47	0.89
*00070+6516	00 09 44.20	+65 33 21.9	118.631671	3.033102	5.11	0.19	−19.81	3.05	6.52	1.26
*00116+6716	00 14 20.10	+67 33 22.0	119.390751	4.939818	1.95	0.22	−7.24	1.84	8.68	0.42
*00289+6327	00 31 51.50	+63 43 58.0	120.767534	0.943341	1.14	0.12	−63.37	1.78	4.8	7.19
*00342+6347	00 37 11.02	+64 04 01.0	121.374013	1.238323	4.32	0.2	−29.18	11.68	30.32	1.87
*00412+6638	00 44 15.34	+66 54 41.1	122.226176	4.049512	2.95	0.2	−5.46	2.43	7.39	0.29
*00455+6137	00 48 33.27	+61 53 36.8	122.592344	−0.97629	1.73	0.17	−46.63	6.34	9.56	3.77
*00468+6527	00 49 55.13	+65 43 41.2	122.775675	2.856825	3.57	0.21	−63.12	4.59	12.61	7.2
*00484+6531	00 51 33.00	+65 47 58.0	122.943481	2.927701	2.77	0.21	−65.47	4.34	16.95	7.52
00519+6535	00 54 52.90	+65 53 55.0	123.284026	3.02922	2.5	0.21	−66.64	4.74	15.65	7.7
*01166+6635	01 20 03.73	+66 51 31.7	125.745473	4.143561	2.19	0.21	−2.01	2.04	9.7	0.07
01584+6706	02 02 17.98	+67 21 23.9	129.689952	5.419357	1.78	0.19	−10.57	15.22	8.7	0.58
*02220+6107	02 25 47.50	+61 20 47.0	133.995193	0.517945	2.6	0.15	−49.37	7.58	13.9	5.77
*02244+6035	02 28 10.40	+60 49 17.0	134.452953	0.131981	1.37	0.15	−14.73	2.12	8.26	0.83
02425+6851	02 47 00.20	+69 04 11.0	132.981891	8.484117	3.59	0.12	−10.33	3.36	16.19	0.57
*02455+6034	02 49 23.20	+60 47 01.0	136.83675	1.136532	8.32	0.23	−42.81	6	13.91	4.75
*02459+6029	02 49 47.30	+60 42 10.1	136.916324	1.08546	9.68	0.12	−40.63	3.2	15.2	4
02485+6902	02 53 07.20	+69 14 36.0	133.396432	8.881912	4.92	0.27	−11.8	13.18	33.03	0.66
02499+6911	02 54 32.30	+69 23 23.0	133.441133	9.069436	6.66	0.19	−15.54	8.6	21.73	0.9
03183+6321	03 22 36.38	+63 32 06.3	138.853953	5.43829	3.78	0.15	−17.76	5.09	36.94	1.07
03211+5446	03 24 59.10	+54 57 25.0	143.828825	−1.560649	7.88	0.2	−32.73	3.15	31.29	2.94
03245+3002	03 27 40.97	+30 12 57.3	158.774061	−21.57275	5.36	0.16	3.17	3.53	10	. . .
03248+6551	03 29 20.46	+66 01 38.8	138.048528	7.905155	2.02	0.16	−3.62	2.36	8.69	0.18
03260+3111	03 29 09.53	+31 22 02.4	158.3008734	−20.463184	11.9	0.34	7.53	4.1	10.4	. . .
03275+5450	03 31 23.40	+55 00 35.0	144.558996	−1.000203	3.39	0.25	−30.54	2.71	17.4	2.57
03463+5331	03 50 08.30	+53 41 00.0	147.540273	−0.424337	2.72	0.18	−8.02	2.11	7.4	0.49
04034+5107	04 07 13.80	+51 15 58.0	151.08813	−0.574353	2.62	0.15	−26.2	6.2	9.54	2.59
04044+5110	04 08 14.40	+51 18 53.0	151.172315	−0.432188	4.25	0.2	−26.2	3.1	10.9	2.63
04088+3834	04 12 12.31	+38 41 59.9	160.326764	−9.182407	2.73	0.2	−3.44	1.78	5.7	0.3
04173+4328	04 20 53.25	+43 36 15.0	158.047386	−4.535014	2.15	0.44	−8.82	4.63	7.4	0.76
04173+4524	04 20 56.60	+45 31 08.0	156.698679	−3.172826	3.15	0.15	−22.87	2.98	15.2	3.09
04271+3502	04 30 25.80	+35 09 13.0	165.472555	−9.058621	5.05	0.3	0.37	7.04	15.7	. . .

Table 1 —*Continued.*

Name	$\alpha(2000)$ (h m s)	$\beta(2000)$ (° ′ ″)	l (°)	b (°)	T_{A}^{*} (K)	T_σ (K)	V_{LSR} (km s^{-1})	δV (km s^{-1})	V_{span} (km s^{-1})	D_k (kpc)
(1)	(2)	(3)	(4)	(5)	(6)	(7)	(8)	(9)	(10)	(11)
04299+2915	04 33 03.80	+29 21 43.0	170.233385	−12.521205	2.54	0.17	3.04	4.98	8.48	. . .
04307+5209	04 34 38.70	+52 15 23.0	153.398895	3.116812	0.94	0.11	−7.96	3.13	5.65	0.57
04319+5056	04 35 50.00	+51 02 38.0	154.41958	2.435062	1.72	0.15	−3.16	2.45	5.2	0.21
04324+5102	04 36 15.92	+51 08 08.1	154.397355	2.546939	4.1	0.14	−37.55	4.9	15.65	6.9
04324+5106	04 36 21.04	+51 12 55.0	154.347282	2.610404	6.74	0.25	−36.02	5.37	12.2	6.48
04335+5110	04 37 24.50	+51 16 32.0	154.41362	2.77363	4.97	0.16	−34.89	3.81	15.6	6.22
04368+2557	04 39 52.92	+26 03 06.8	173.8215694	−13.527364	1.87	0.14	4.51	4.71	8.26	. . .
04381+2540	04 41 12.69	+25 46 35.5	174.2357869	−13.472849	2.63	0.21	6.12	2.03	4.8	. . .
04587+4411	05 02 20.20	+44 16 03.0	162.47734	1.50271	2.37	0.17	−0.64	5.27	7.5	0.04
05075+3755	05 10 59.98	+37 59 27.2	168.471492	−0.972151	1.29	0.17	−33.51	14.25	18.69	29.82
05236+0620	05 26 18.36	+06 22 57.1	197.05278	−15.68507	0.73	0.14	−4.53	2.21	3.04	. . .
05335+3609	05 36 53.23	+36 10 50.9	172.877253	2.270042	6.55	0.15	−16.79	6.1	11.7	15.18
05356−0530	05 38 06.50	−05 28 54.0	209.4348116	−18.796256	4.53	0.13	5.11	4.28	40.85	0.36
05363+3127	05 39 35.85	+31 29 12.2	177.146733	0.237072	3.03	0.13	−1.09	5.42	7.39	0.65
05366+3601	05 40 02.50	+36 03 31.0	173.320658	2.743877	4.35	0.18	−20.34	4.83	13.91	. . .
05375+3536	05 40 52.50	+35 38 24.0	173.765722	2.665709	10.9	0.22	−17.71	3.32	14.34	26.76
05375+3540	05 40 52.90	+35 42 16.7	173.711494	2.701006	12.6	0.26	−16.64	4.86	30	20.98
05379+3515	05 41 19.20	+35 16 46.0	174.120141	2.552314	3.3	0.18	−17.67	6.32	15.21	. . .
05381−0921	05 40 34.30	−09 20 08.0	213.3860117	−19.950587	6.68	0.15	1.56	4.8	18.26	0.08
05387−0924	05 41 04.13	−09 23 19.5	213.4933593	−19.862943	5.37	0.17	2.86	2.68	9.6	0.17
05394−0151	05 41 58.50	−01 50 24.0	206.5052375	−16.268355	18.4	0.16	8.61	4.99	15.21	0.67
05399+2631	05 43 03.00	+26 33 00.0	181.73645	−1.732799	1.26	0.18	−2.62	2.09	9.1	. . .
05399−0121	05 42 27.70	−01 20 02.0	206.0084668	−15.924558	7.86	0.17	7.62	5.45	20.86	0.59
05399−1001	05 42 19.10	−10 00 08.0	214.2230027	−19.848847	3.19	0.3	1.46	2.12	10	0.07
05404−0220	05 43 00.57	−02 18 45.4	207.0662752	−16.259142	3.82	0.2	8.77	2.98	12.17	0.68
05411+3302	05 44 24.82	+33 03 31.0	176.347927	1.930962	1.84	0.23	−9.39	3.96	17	18.94
05413−0104	05 43 51.50	−01 02 52.0	206.0054854	−15.482164	5.81	0.19	5.2	8.84	28.25	0.39
05437−0343	05 46 14.80	−03 41 58.0	208.7359072	−16.180012	3.19	0.22	9.1	3.93	8.69	0.67
05445+0020	05 47 05.01	+00 21 47.2	205.1093819	−14.107369	10.8	0.37	9.9	8.38	29.6	0.81
05462−0124	05 48 47.21	−01 23 52.3	206.9210946	−14.555896	2.43	0.22	7.33	9.16	12.48	0.55
05575+2141	06 00 35.26	+21 41 11.8	187.961159	−0.772756	1.51	0.13	−0.78	7.38	28.25	. . .
06084−0611	06 10 51.31	−06 11 54.0	213.8826992	−11.834592	6.68	0.19	13.97	3.11	17.8	0.94
06102+1537	06 13 04.60	+15 36 31.0	194.710338	−1.152557	3.48	0.2	15.1	5.27	11.3	3.32
06281+1039	06 30 50.30	+10 37 22.0	201.143823	0.317507	4.02	0.25	5.41	2.49	10.4	0.45
06282+0423	06 30 52.44	+04 21 24.5	206.705413	−2.572085	4.06	0.21	12.37	10.46	22.16	0.94
06294+0352	06 32 07.52	+03 50 07.5	207.312536	−2.535412	5.32	0.32	15.99	2.38	10.4	1.26
06308+0402	06 33 31.10	+04 00 07.0	207.324606	−2.150318	6.91	0.13	14.34	3.06	15.21	1.1
06318+0420	06 34 32.54	+04 17 52.1	207.179248	−1.78752	3.6	0.18	11.52	5.5	14.77	0.85
06343+0425	06 37 00.80	+04 23 04.0	207.385365	−1.200596	1.99	0.16	4.66	2.02	10	0.3
06373+1053	06 40 05.70	+10 51 10.0	201.985033	2.442405	2.56	0.34	8.17	1.73	8.3	0.69
06423+0006	06 44 52.90	+00 03 33.0	212.131769	−1.431586	1.14	0.22	44.34	5.84	7.78	6.71
06425+0038	06 45 07.50	+00 35 36.0	211.684076	−1.133751	2.14	0.17	41.47	7.3	11.3	6.21
06511−0507	06 53 36.78	−05 11 15.0	217.79789	−1.880434	1.24	0.2	31.68	4.92	6.95	2.53
06545−0251	06 57 02.20	−02 55 51.0	216.178333	−0.091748	2.8	0.1	22.41	2.69	10.43	1.52
07100−1110	07 12 24.47	−11 15 33.5	225.326443	−0.531399	3.01	0.16	17.02	3.59	13.5	0.98
07157−1830	07 17 56.30	−18 36 21.0	232.456019	−2.760925	1.59	0.19	33.62	2.62	6.09	2.2
07221−2544	07 24 12.90	−25 49 58.0	239.54154	−4.848271	4.21	0.22	24.27	4.46	13	1.54
07297−1926	07 31 58.30	−19 32 31.0	234.851753	−0.284031	0.76	0.18	40.78	3.47	3.91	2.93
08004−2815	08 02 30.10	−28 24 01.0	246.013009	1.260662	2.42	0.34	54.63	13.22	15.21	5.44
17207−3404	17 24 04.20	−34 07 12.0	353.15702	1.05134	7.65	0.22	8.45	9.72	36.95	21.81
17364−1946	17 39 23.50	−19 47 51.0	7.05197	5.99769	4.11	0.2	8.08	7.14	14.78	15.22
17369−1945	17 39 56.00	−19 46 36.0	7.13702	5.90015	2.93	0.21	10.2	2.26	4.4	14.81
17392−3309	17 42 34.40	−33 10 37.0	356.04489	−1.66466	3.13	0.27	−1.09	8.49	11.3	16.51
17419−3150	17 45 12.20	−31 51 22.0	357.46099	−1.4453	1.88	0.2	−0.7	14.06	16.85	16.54
17520−2731	17 55 14.20	−27 32 25.0	2.28423	−1.10303	2.3	0.42	0.4	3.9	7	16.69
17555−2136	17 58 33.00	−21 36 19.0	7.79598	1.22415	3.01	0.2	22.02	6.51	17.82	13.17

Table 1 —*Continued.*

Name	α(2000) (h m s)	β(2000) (° ′ ″)	l (°)	b (°)	T_A^* (K)	T_σ (K)	$V_{\rm LSR}$ (km s^{-1})	δV (km s^{-1})	$V_{\rm span}$ (km s^{-1})	D_k (kpc)
(1)	(2)	(3)	(4)	(5)	(6)	(7)	(8)	(9)	(10)	(11)
18111−2028	18 14 05.00	−20 27 56.0	10.56027	−1.38257	1.55	0.24	32.21	6.4	24.77	−12.79
18134−1942	18 16 21.60	−19 41 31.3	11.49535	−1.48395	11.5	0.4	9.16	5.37	20.86	15.41
18136−1347	18 16 28.60	−13 46 33.0	16.71365	1.30475	6.64	0.22	18.93	4.86	9.13	14.47
18148−0440	18 17 29.80	−04 39 38.0	24.88448	5.38459	1.96	0.09	8.08	1.84	3.91	14.88
18188−1631	18 21 43.10	−16 30 00.0	14.91099	−1.09768	6.16	0.43	22.04	4.57	24.34	14.14
18273+0034	18 29 53.06	+00 36 06.4	31.00628	5.06938	3.1	0.35	6.97	2.7	8.3	14.16
18282−1529	18 31 09.70	−15 27 32.0	16.88971	−2.62209	4.78	0.24	17.05	2.98	6.51	14.65
18316−0602	18 34 20.84	−05 59 42.4	25.6494	1.04977	5.2	0.28	43.38	15.26	23.91	12.38
18385−0755	18 41 17.90	−07 52 51.0	24.76566	−1.34825	1.73	0.23	54.49	8.82	14.78	11.77
18473+0131	18 49 55.60	+01 35 04.0	34.170041	1.058437	2.3	0.27	91.73	7.35	17.38	7.96
18532+0420	18 55 45.40	+04 24 47.0	37.351628	1.052219	1.81	0.19	9.77	2.95	13	12.92
18567+0700	18 59 13.60	+07 04 47.0	40.119071	1.500643	7.98	0.33	28.52	3.07	12.6	11.36
18572+0057	18 59 49.00	+01 01 34.0	34.800828	−1.395936	4.9	0.15	41.95	12.96	27.39	11.45
18583+0136	19 00 55.60	+01 40 58.0	35.511907	−1.342749	5.16	0.17	30.3	5.02	23.91	12.05
19207+1809	19 23 01.10	+18 14 59.0	52.70594	1.52982	2.12	0.19	21.34	2.05	6.96	8.96
19223+1826	19 24 35.10	+18 32 16.0	53.13552	1.33831	2.47	0.16	20.62	1.45	3.48	8.89
19258+1919	19 28 00.30	+19 25 15.0	54.29695	1.0465	2.15	0.16	−49.35	3.47	7.82	14.83
19300+2158	19 32 13.49	+22 04 56.6	57.10624	1.45707	2.01	0.35	−61.84	3.98	7.8	16.25
19387+2658	19 40 48.80	+27 05 10.0	62.42938	2.19102	0.97	0.25	4.99	3.5	6.1	7.46
19407+2454	19 42 49.30	+25 01 41.0	60.86387	0.78037	1.38	0.17	9.78	2.5	3.48	7.54
19408+2554	19 42 54.10	+26 01 22.0	61.73622	1.25897	3.42	0.16	3.64	2.03	5.21	7.74
19413+2349	19 43 27.78	+23 56 53.5	59.9997	0.11656	8.06	0.15	21.1	2.33	14.35	6.89
19454+2625	19 47 31.70	+26 33 17.0	62.71595	0.62746	1.33	0.15	0.64	7.61	12.6	7.69
19457+2357	19 47 55.10	+24 04 45.0	60.623325	−0.698201	3.4	0.21	28.59	3.22	5.65	5.89
19458+2442	19 48 00.14	+24 50 18.6	61.288383	−0.331204	3.59	0.13	−12.69	6.64	9.99	8.95
19508+2705	19 52 54.80	+27 13 43.0	63.907111	−0.063466	1.5	0.16	−16.68	11.31	16.08	8.57
19560+3135	19 58 03.14	+31 44 07.0	68.341878	1.313376	1.79	0.28	−65.02	5.81	14.4	13.85
20016+3243	20 03 34.30	+32 52 13.0	69.921521	0.920929	1.4	0.12	15.32	4.89	6.52	3.78
20033+2848	20 05 23.90	+28 56 42.0	66.812815	−1.507827	5.39	0.13	10.48	2.94	13.48	5.7
20050+2720	20 07 06.70	+27 28 53.0	65.780227	−2.612263	2.17	0.15	4.07	8.29	13.47	6.59
20051+3016	20 07 06.70	+30 25 09.0	68.256233	−1.029066	2.25	0.14	7.37	3.07	12.17	5.55
20051+3435	20 07 04.50	+34 44 45.0	71.895364	1.311607	5.5	0.16	9.53	6.56	18.69	4.03
20068+3328	20 08 49.91	+33 37 32.2	71.149824	0.399907	3.74	0.26	−17.43	2.79	7.8	6.84
20072+2720	20 09 20.10	+27 29 25.0	66.054422	−3.022408	3.11	0.16	4.62	5.37	13.48	6.47
20078+3254	20 09 49.70	+33 03 19.0	70.784484	−0.084988	1.29	0.17	8.64	6.09	14.34	4.58
20184+3936	20 20 15.10	+39 45 36.0	77.524535	1.896355	3.44	0.14	1.22	4.95	14.34	3.35
20190+4011	20 20 49.30	+40 20 48.0	78.070124	2.138794	2.18	0.13	12.5	1.69	3.91	...
20190+4102	20 20 47.50	+41 12 06.8	78.772125	2.628169	8.2	0.14	1.85	2.76	10.86	2.82
20197+3745	20 21 38.80	+37 55 06.0	76.16238	0.627096	2.44	0.19	5.23	3.6	12.2	3.1
20227+4154	20 24 31.40	+42 04 17.0	79.88505	2.55185	5.28	0.21	5.7	5.73	27	...
20228+4215	20 24 34.40	+42 25 01.0	80.17348	2.74284	12.5	0.17	3.96	3.34	15.22	...
20243+3752	20 26 10.35	+38 02 42.1	76.77831	−0.02992	2.88	0.21	−2.41	6.24	11.73	4.06
20243+3853	20 26 11.61	+39 03 32.8	77.60721	0.55431	4.72	0.21	7.88	5	15.21	...
20274+4219	20 29 12.90	+42 29 45.0	80.7348	2.09116	1.73	0.11	−6.6	4.61	11.3	3.54
20275+4001	20 29 24.90	+40 11 21.0	78.88707	0.70905	6.91	0.17	−6.63	3.65	26.5	3.96
20285+3939	20 30 20.43	+39 49 34.1	78.69743	0.35234	3.56	0.17	8.89	2.6	6.65	...
20290+4052	20 30 50.80	+41 02 25.0	79.73534	0.98979	3.72	0.34	−2.88	4.63	7.83	3.31
20293+3952	20 31 12.90	+40 03 21.0	78.9818	0.35239	3.28	0.17	5.77	14.1	31.7	2
20300+3909	20 31 52.40	+39 19 33.0	78.46799	−0.18141	3.23	0.2	7.24	2.37	13.5	...
20300+4058	20 31 49.90	+41 09 00.0	79.93352	0.90487	3.62	0.21	11.98	2.99	6.5	...
20306+4005	20 32 27.92	+40 16 08.2	79.29496	0.28601	4.09	0.18	0.06	5.02	13.91	2.99
20309+4257	20 32 38.90	+43 07 32.0	81.61517	1.95351	1.89	0.16	−10.07	3.16	5.65	3.72
20321+4112	20 33 55.12	+41 22 49.5	80.35193	0.72635	3.85	0.27	−2.25	7.9	19.99	3.05
20322+4031	20 34 06.40	+40 41 22.0	79.81866	0.28551	2.6	0.18	8.94	2.08	7.4	...
20329+3846	20 34 48.40	+38 56 49.0	78.50218	−0.864	4.73	0.35	4.83	17.09	24.34	1.98

Table 1 —*Continued.*

| Name	$\alpha(2000)$ (h m s)	$\beta(2000)$ (° ′ ″)	l (°)	b (°)	T_A^* (K)	T_σ (K)	V_{LSR} (km s^{-1})	δV (km s^{-1})	V_{span} (km s^{-1})	D_k (kpc)
(1)	(2)	(3)	(4)	(5)	(6)	(7)	(8)	(9)	(10)	(11)
20332+4124	20 35 00.50	+41 34 48.0	80.63395	0.68206	6.75	0.45	−3.44	5.16	11.3	3.15
20333+4102	20 35 09.50	+41 13 18.0	80.36393	0.44481	5.14	0.26	−33.78	17.9	34.33	6.12
20343+4129	20 36 07.10	+41 40 01.0	80.82803	0.56836	4.52	0.18	11.67	3.21	22.6	. . .
20346+4706	20 36 15.90	+47 16 48.0	85.33469	3.9201	4.13	0.16	0.31	2.77	9.1	. . .
20350+4126	20 36 52.60	+41 36 33.0	80.86728	0.42046	6.67	0.41	−2.85	5.29	15.21	3
20364+3816	20 38 20.00	+38 27 06.0	78.52138	−1.71157	3.14	0.16	0	9.98	16.95	3.23
20436+5849	20 44 49.25	+59 00 18.1	95.53324	9.97828	2.4	0.2	−2.77	3.31	12.6	0.43
20489+4410	20 50 43.20	+44 21 59.0	84.5993	0.14062	6.1	0.23	3.03	3.87	13.5	. . .
20527+4957	20 54 22.20	+50 08 53.0	89.44418	3.36011	1.25	0.16	5.52	3.8	7	. . .
20550+5158	20 56 32.10	+52 10 09.0	91.21236	4.40319	2.08	0.14	−4.33	9.04	13.48	1.11
20553+5208	20 56 53.10	+52 20 06.0	91.37395	4.46961	4.38	0.23	−8.24	3.96	21.3	1.71
20565+5003	20 58 10.95	+50 15 07.2	89.91898	2.96227	1.49	0.14	−0.59	4.38	10.4	. . .
20582+7724	20 57 11.70	+77 35 47.9	111.66994	20.22046	1.73	0.25	−8.62	2.31	4.3	0.69
20588+5215	21 00 21.20	+52 27 09.0	91.809158	4.144649	4.43	0.38	−0.66	4.32	7.4	. . .
21005+5217	21 02 05.50	+52 28 54.0	92.005844	3.964499	2.62	0.31	−4.43	2.71	13	1.03
21007+4847	21 02 26.22	+48 59 37.5	89.423433	1.615789	2.94	0.19	−72.81	4.07	12.6	10.68
21007+5036	21 02 21.79	+50 48 34.7	90.77693	2.82765	4.63	0.26	−10.08	4.05	17.4	2.03
21020+4939	21 03 42.30	+49 51 53.0	90.2118	2.04031	1.68	0.21	−3.37	3.17	11.74	1.04
21025+4912	21 04 15.40	+49 24 25.0	89.92983	1.66867	2.61	0.17	−74.41	2.81	5.65	10.78
21036+4927	21 05 14.73	+49 39 53.1	90.22895	1.72159	2.52	0.21	3.68	14.95	19.99	. . .
21101+5150	21 11 42.40	+52 03 15.0	92.67952	2.58843	2.7	0.17	−13.39	3.45	27.81	2.16
21106+5206	21 12 12.20	+52 18 31.0	92.91732	2.70721	2.47	0.27	−10.93	3.72	7	1.85
21131+5221	21 14 45.10	+52 33 56.0	93.37155	2.60245	5.59	0.15	−7.33	10.16	34.77	1.35
21136+5317	21 15 11.00	+53 30 30.0	94.09809	3.20788	1.59	0.19	−3.27	7.34	9.13	0.61
21169+6804	21 17 38.52	+68 17 34.2	105.16593	13.15667	2.86	0.17	2.01	1.77	10.87	. . .
21182+4641	21 20 04.70	+46 54 43.0	89.92545	−1.96175	5.55	0.18	2.02	2.27	9.1	. . .
21184+5507	21 19 58.60	+55 19 52.0	95.89396	3.97984	2.03	0.24	−80.09	2.83	4.34	10.73
21202+5157	21 21 59.80	+52 10 56.9	93.87299	1.54495	5.11	0.26	−60.11	3.68	14.4	7.8
21207+5338	21 22 23.40	+53 51 49.0	95.10064	2.69591	2.01	0.13	−3.83	2.7	5.65	0.64
21307+5049	21 32 31.50	+51 02 22.0	94.2617	−0.41114	2.97	0.13	−47.98	3.53	7.39	5.28
21334+5039	21 35 09.20	+50 53 09.0	94.46296	−0.80404	4.65	0.15	−45.32	3.44	10	4.95
21340+5339	21 35 43.90	+53 52 59.0	96.541839	1.356916	5.22	0.37	−69.49	3.41	11.3	9.31
21360+5607	21 37 38.84	+56 21 21.3	98.40111	3.011709	2	0.21	5.51	1.58	5.2	. . .
21379+5106	21 39 41.12	+51 20 35.6	95.298186	−0.937454	4.68	0.25	−42.26	9.25	33.47	4.53
21498+7053	21 50 40.14	+71 07 46.7	109.298672	13.215891	3.01	0.18	−11.36	3.15	11.74	0.92
21548+5747	21 56 29.70	+58 01 35.0	101.433682	2.6534	3.83	0.17	−2.11	3.07	9.99	0.16
*22045+5800	22 06 13.80	+58 15 28.0	102.59963	2.064894	3.06	0.19	−27.73	2.47	16.51	2.52
22126+7443	22 13 19.76	+74 58 24.0	113.085841	15.213202	1.67	0.2	−6.3	4.12	5.65	0.44
22199+6322	22 21 30.20	+63 36 23.0	107.164645	5.423008	6.82	0.17	−9.49	5.64	10.4	0.78
*22202+6317	22 21 55.80	+63 32 39.0	107.170717	5.34498	5.84	0.14	−10.81	6.02	11.73	0.89
*22262+5938	22 28 06.40	+59 53 53.0	105.848255	1.868516	1.35	0.18	−12.98	2.95	3.91	1.12
*22321+5829	22 34 02.00	+58 44 39.0	105.90725	0.49037	3.12	0.19	−52.63	3.11	14.8	4.91
*22345+5917	22 36 24.00	+59 32 42.0	106.569534	1.033382	5.05	0.23	−12.65	4.33	9.12	1.06
*22528+5936	22 54 49.61	+59 52 48.1	108.782348	0.251085	5.24	0.19	−52.94	4.55	12.6	4.87
*22567+6113	22 58 47.90	+61 30 04.0	109.913964	1.509566	2.54	0.15	−7.44	1.81	7.4	0.55
*23065+5927	23 08 39.20	+59 44 04.0	110.308161	−0.594135	4.64	0.21	−36.27	5.87	17.8	2.76
*23077+5925	23 09 54.80	+59 41 55.0	110.441108	−0.688177	2.41	0.23	−51.38	2.38	14.3	4.52
*23079+5932	23 10 03.60	+59 48 24.0	110.499383	−0.595324	4.37	0.17	−52.74	3.46	16.51	4.8
*23091+6211	23 11 15.96	+62 27 34.5	111.6394	1.804636	5.36	0.24	−10.91	1.59	5.21	0.78
*23215+5826	23 23 48.70	+58 43 15.0	111.753786	−2.236154	5.87	0.14	−47	3.02	25.2	3.81
*23330+6437	23 35 23.41	+64 54 29.1	114.978684	3.217181	4.28	0.2	−64.54	2.95	8.25	7.42
*23331+6523	23 35 27.60	+65 39 42.0	115.204924	3.936178	2.75	0.2	−24.94	3.96	7.8	1.7
*23486+5958	23 51 05.70	+60 15 11.0	115.50882	−1.74603	1.76	0.23	−3.45	3.87	6.52	0.19
23494+6155	23 51 54.10	+62 11 58.0	116.051402	0.125665	0.86	0.15	−49.29	9.28	8.26	4.1
23500+6729	23 52 27.80	+67 46 24.0	117.3816	5.53945	2.16	0.19	−6.84	2.05	3.5	0.41
*23504+6012	23 52 58.20	+60 28 45.0	115.7862	−1.57878	2.03	0.21	−39.08	7.04	10	2.81
*23592+6716	00 01 49.50	+67 32 59.0	118.20797	5.13425	5.5	0.17	−16.51	4.61	16.51	1.05
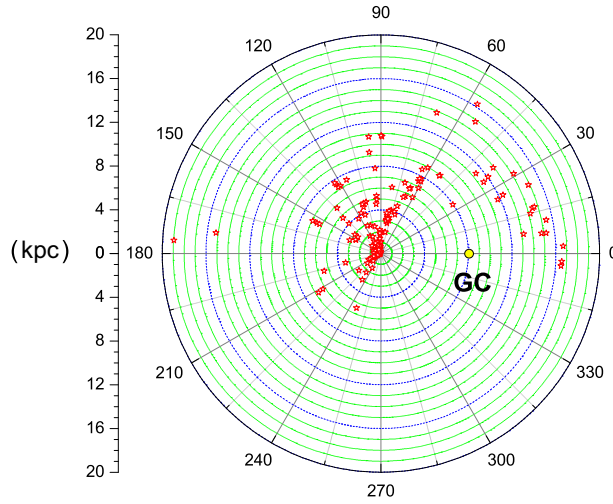
Fig. 3 Projected Galactocentric distribution of the 201 candidates.

The kinematic distances of the CO sources are plotted in Figure 3. The lack of the inner part of the Galaxy is obvious. Because of serious contamination in the CO line, we do not observe these sources in this region ($|b| < 1°$ when $l \leq 60°$ or $l \geq 300°$). We could investigate examples of molecular emission, such as high density tracers, around these sources in further observations.

Figure 4 demonstrates the $L - V_{\mathrm{LSR}}$ diagram for all the CO sources that we selected. The range of the V_{LSR} is from 91.73 to –80.09 km s^{-1}. The distribution of V_{LSR} confirms the distribution of the 1331 sources from the sample given by Yang et al. (2002). It basically follows the Galactic rotation. A significant part of the sources, associated with the star-forming regions, is distributed over a large fraction of the Galactic plane. A large portion of the sources is located in the second Galactic quadrant. Some of them with negative radial velocities and large amplitudes are possibly located in the Perseus arm.

The statistical distribution of the peak antenna temperature for the 201 sources is illustrated in Figure 5. The antenna temperature ranges from 0.73 to 18.4 K and the average temperature is 3.8 K. The distribution of the line intensity is unimodal, generally from 2 K to 10 K, and the peak lies in 2–3 K. The source *IRAS* 05394–0151 is detected with the highest antenna temperature of 18.4 K.

We also use *IRAS* PSC and *MSX* PSC to investigate if there are infrared sources around these CO sources within 5′.

Table 2 displays the number of *IRAS* point sources and *MSX* point sources around the 201 sources, and denotes the association of the *IRAS* point source and *MSX* point source by "n" or "a" tag. Column (1) is the *IRAS* name, Cols. (2) and (3) give the number of *IRAS* point sources and *MSX* point sources respectively in the region within 5′ of the center of this sample of sources. Column (4) denotes the association between Cols. (2) and (3). Label a represents the overlap of an *MSX* point source with our selected CO source. Label n means that there is no *MSX* source in the position of the central source. Columns (4) and (5) denote the type and identification of these 201 observed sources.

4.2 CO and its Isotope Molecule Emission from Sources

A complete set of ^{12}CO(1–0), ^{13}CO(1–0) and C^{18}O(1–0) line emissions toward 201 sources is published online. The ^{12}CO(1–0), ^{13}CO(1–0) and C^{18}O(1–0) spectra are plotted in blue, green and red respectively. These sources are classified into four types of possible cloud-cloud collision region candidates. Type 1 illustrates that lines with different optical thickness for each source have a similar profile. The ^{12}CO, ^{13}CO and C^{18}O(J=1–0) spectra have a double-peaked or multi-peaked main line

Table 2 Detected *IRAS* and *MSX* Sources around the Selected Sources

Name	*IRAS* Point Source	*MSX* Point Source	Note	Type	Identification
		(Sky coverage within 5′)			
(1)	(2)	(3)	(4)	(5)	(6)
00021+6604	2	0		IR	
00056+6605	1	1	n	IR	
00070+6516	1	1	a	IR	
00116+6716	1	0		IR	
00289+6327	1	1	a	IR	
00342+6347	2	1	a	IR	
00412+6638	1	2	n	G	2MASX J00441534+6654411
00455+6137	2	2	n	IR	
00468+6527	1	2	n	YSO	45P 26
00484+6531	2	1	a	IR	
00519+6535	3	2	a	HII	SH 2-183
01166+6635	1	0		IR	
01584+6706	1	0		G	2MFGC 01551
02220+6107	1	0		IR	
02244+6035	2	0		DNe	LDN 1365
02425+6851	1	0		IR	
02455+6034	2	16	a	HII	
02459+6029	2	12	a	HII	KSP2003] J024947.30+604210.1
02485+6902	2	0		IR	
02499+6911	2	0		IR	
03183+6321	2	0		G	2MASX J03223621+6332054
03211+5446	4	3	n	HII	
03245+3002	2	0		IR	
03248+6551	1	0		G	2MASX J03292042+6601389
03260+3111	3	1	a	IR	NGC 1333 NED01
03275+5450	1	1	a	IR	
03463+5331	1	0		IR	
04034+5107	2	2	n	IR	
04044+5110	3	0		IR	
04088+3834	3	0		IR	
04173+4328	1	0		G	2MASX J04205315+4336158
04173+4524	1	0		IR	
04271+3502	1	0		IR	
04299+2915	1	0		IR	
04307+5209	1	0		IR	
04319+5056	1	0		IR	
04324+5102	2	2	a	IR	2MASX J04361587+5108075
04324+5106	2	3	a	IR	2MASX J04362105+5112546
04335+5110	1	0		IR	
04368+2557	2	0		IR	
04381+2540	1	0		IR	2MASX J04411273+2546360
04587+4411	1	2	n	IR	
05075+3755	1	4	n	IR	B2 0507+37
05236+0620	1	0		G	2MASX J05261836+0622571
05335+3609	1	1	a	G	2MASX J05365322+3610508
05356−0530	2	1	a	IR	
05363+3127	1	0		IR	
05366+3601	3	3	a	IR	
05375+3536	2	6	a	IR	
05375+3540	3	9	a	HII	WN B0537.5+3540
05379+3515	1	0		IR	
05381−0921	2	0		IR	
05387−0924	1	0		Or*	V* V1792 Ori
05394−0151	8	7	n	IR	
05399+2631	1	0		IR	
05399−0121	1	0		YSO	JCMTSF J054227.9−012003
05399−1001	3	0		IR	

Table 2 —*Continued.*

Name	*IRAS* Point Source	*MSX* Point Source	Note	Type	Identification
		(Sky coverage within 5′)			
(1)	(2)	(3)	(4)	(5)	(6)
05404−0220	1	0		Em*	HD 38087
05411+3302	1	0		G	2MASX J05442482+3303312
05413−0104	2	0		IR	
05437−0343	1	0		IR	
05445+0020	4	0		HII	NGC 2071 NED01
05462−0124	2	0		IR	
05575+2141	1	0		IR	
06084−0611	3	4	n	IR	
06102+1537	1	0		IR	
06281+1039	1	2	a	Rne	NAME Steine GN J0630.8+1037
06282+0423	4	6	a	IR	
06294+0352	1	1	n	YSO	2MASS J06320752+0350075
06308+0402	1	11	a	YSO	
06318+0420	4	11	a	IR	
06343+0425	2	1	a	IR	
06373+1053	2	0		IR	
06423+0006	1	2	n	IR	
06425+0038	1	0		IR	
06511−0507	1	0		IR	
06545−0251	1	0		IR	
07100−1110	1	1	a	G	2MASX J07122445−1115336
07157−1830	2	1	n	IR	
07221−2544	3	2	n	ISM	BRAN 23
07297−1926	3	2	n	IR	
08004−2815	2	5	a	ISM	BRAN 98
17207−3404	3	38	a	IR	
17364−1946	1	0		IR	
17369−1945	1	0		IR	
17392−3309	3	11	n	IR	
17419−3150	3	13	a	IR	
17520−2731	5	14	n	IR	
17555−2136	1	9	n	IR	
18111−2028	2	8	n	IR	
18134−1942	1	9	a	HII	
18136−1347	1	4	a	HII	
18148−0440	1	1	a	YSO	NAME LDN 483 FIR
18188−1631	3	8	n	IR	
18273+0034	2	1	a	COR	
18282−1529	2	8	n	IR	
18316−0602	1	12	a	HII	GAL 025.65+01.05
18385−0755	2	9	n	IR	
18473+0131	3	9	n	IR	
18532+0420	3	7	a	IR	
18567+0700	2	11	a	HII	SH 2−75
18572+0057	2	4	n	IR	
18583+0136	2	6	n	IR	
19207+1809	1	4	a	IR	
19223+1826	2	5	a	IR	
19258+1919	2	0		IR	
19300+2158	2	6	a	YSO	2MASS J19321348+2204566
19387+2658	2	2	a	IR	
19407+2454	2	2	a	IR	
19408+2554	2	4	a	IR	
19413+2349	2	8	a	IR	
19454+2625	3	5	n	IR	
19457+2357	2	4	a	IR	
19458+2442	3	13	a	Radio	

Table 2 —*Continued.*

Name	IRAS Point Source (Sky coverage within 5′)	MSX Point Source	Note	Type	Identification
(1)	(2)	(3)	(4)	(5)	(6)
19508+2705	3	6	n	IR	
19560+3135	2	5	a	IR	
20016+3243	1	0		IR	
20033+2848	3	1	a	IR	
20050+2720	2	4	a	COR	
20051+3016	3	4	a	IR	
20051+3435	1	6	a	Star	
20068+3328	1	12	a	IR	
20072+2720	3	2	n	IR	
20078+3254	3	8	a	IR	
20184+3936	1	8	a	IR	
20190+4011	2	9	n	IR	
20190+4102	1	6	a	G	2MASX J20204749+4112067
20197+3745	3	13	a	IR	
20227+4154	3	1	a	HII	
20228+4215	1	11	a	IR	
20243+3752	2	3	n	RadioS	B2 2024+37
20243+3853	3	5	a	RadioS	
20274+4219	1	0		IR	
20275+4001	3	15	a	YSO	
20285+3939	3	10	a	RadioS	
20290+4052	1	6	a	IR	
20293+3952	1	2	n	IR	
20300+3909	2	11	a	IR	
20300+4058	4	22	a	IR	
20306+4005	2	27	a	G	2MASX J20322791+4016081
20309+4257	2	6	n	IR	
20321+4112	4	8	a	RadioS	18P 61
20322+4031	1	6	a	IR	
20329+3846	1	3	n	IR	
20332+4124	2	10	a	IR	
20333+4102	4	16	a	IR	
20343+4129	1	6	a	IR	
20346+4706	2	2	n	IR	
20350+4126	5	22	a	HII	
20364+3816	1	0		IR	
20436+5849	3	0		IR	
20489+4410	5	11	a	Cloud	JCMTSF J205042.8+442157
20527+4957	2	3	n	IR	
20550+5158	1	0		IR	
20553+5208	1	1	a	IR	
20565+5003	2	4	a	IR	
20582+7724	1	0		IR	
20588+5215	3	1	a	TT*	2MASS J21002140+5227094
21005+5217	1	2	a	IR	
21007+4847	5	0		RadioS	
21007+5036	1	1	a	G	2MASX J21022178+5048346
21020+4939	1	2	n	IR	
21025+4912	2	0		IR	
21036+4927	3	5	a	HII	
21101+5150	2	0		IR	
21106+5206	2	1	n	IR	
21131+5221	1	1	a	IR	
21136+5317	2	1	n	IR	
21169+6804	1	0		IR	2MASX J21173843+6817340
21182+4641	2	0		IR	
21184+5507	1	2	n	IR	

Table 2 —*Continued.*

Name	*IRAS* Point Source	*MSX* Point Source	Note	Type	Identification
	(Sky coverage within 5′)				
(1)	(2)	(3)	(4)	(5)	(6)
21202+5157	6	5	n	RadioS	
21207+5338	1	0		IR	
21307+5049	1	1	a	IR	
21334+5039	2	3	a	HII	2MASS J21350991+5053048
21340+5339	4	6	a	IR	
21360+5607	2	0		IR	
21379+5106	1	2	a	G	2MASX J21394111+5120356
21498+7053	1	0		G	2MASX J21504014+7107468
21548+5747	1	5	n	IR	
22045+5800	2	1	a	IR	
22126+7443	1	0		G	2MASX J22131981+7458237
22199+6322	4	0		Dne	LDN 1204B
22202+6317	2	0		IR	
22262+5938	3	0		IR	
22321+5829	1	4	a	PN	PN PM 1−338
22345+5917	1	1	a	IR	
22528+5936	1	1	a	G	2MASX J22544960+5952481
22567+6113	1	2	n	IR	
23065+5927	1	4	a	IR	
23077+5925	1	12	a	IR	
23079+5932	1	4	a	IR	
23091+6211	2	1	a	Em*	2MASS J23111596+6227344
23215+5826	2	1	a	IR	
23330+6437	2	5	a	G	2MASX J23352340+6454290
23331+6523	2	0		IR	
23486+5958	1	0		IR	
23494+6155	2	1	a	IR	
23500+6729	2	0		IR	
23504+6012	1	10	a	IR	
23592+6716	4	3	n	IR	

Notes: * means the classification of the object comes from SIMBAD.

and the peaks are almost located at the same velocity. It contains 38 sources. Several reasons could induce the double-peaked line profile in optically thick ^{12}CO lines, which include self-absorption, outflow, infall, rotation and a two cloud configuration. People have already compared the spectral profile of ^{12}CO with that of ^{13}CO and $C^{18}O$, and they summarize the feature in different situations (Wang et al. 2004; Dobashi et al. 1993; Walsh et al. 2002; Xin & Wang 2008). Toward this type of source, and the profile of the optically thick ^{12}CO lines fits the profiles of the optically thin ^{13}CO and $C^{18}O$ very well. So the possibility of self-absorption, outflow, infall and rotation is remote. It could be the two separate clouds in the double-peaked profile region. We need to conduct a multi-wavelength investigation toward these possible cloud-cloud collision regions in the future. In type 2, the $C^{18}O(J{=}1$–0) spectra have bad SNR toward these 71 sources. However, the profile of the optically thick ^{12}CO lines also fits the profiles of the optically thin ^{13}CO well, and also shows a double-peaked or multi-peaked profile. This type of source is still treated as a possible cloud-cloud collision candidate. Type 3 contains the spectra with ^{12}CO double-peaked or multi-peaked main lines, and the profiles of the ^{13}CO and $C^{18}O$ lines partly fit the profile of the ^{12}CO line. Considering the uncertainty in the factors, these sources cannot be identified as non cloud-cloud collision candidates; we need further observations toward these 58 sources to confirm this identification. The last 34 sources are plotted in type 4. One set of these sources shows the ^{13}CO, $C^{18}O$ and ^{12}CO lines with a single peak. The other sources present the ^{13}CO and $C^{18}O$ lines with a single peak, and the peak is located between the double peak of the optically thick ^{12}CO lines. It suggests that this type
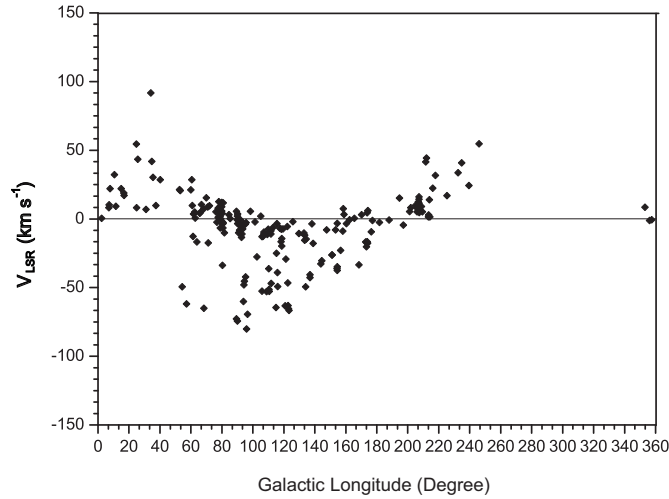
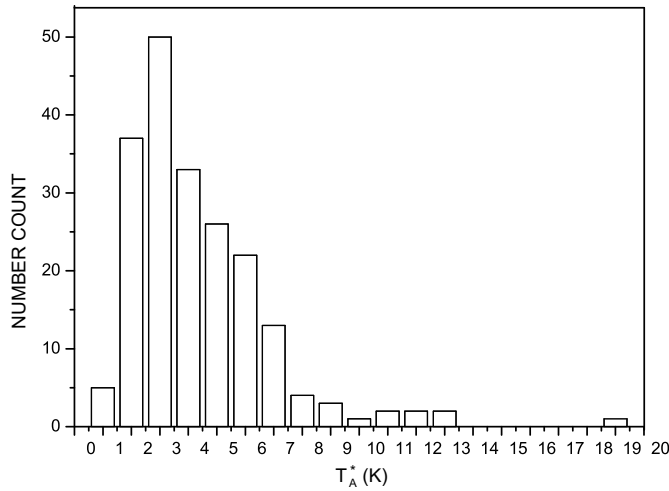**Fig. 4** L-V distribution of our survey sample.

Fig. 5 Statistical distribution of T_A^* for the 201 sources.

of optically thick profile might be induced by self-absorption, infall, etc (Wang et al. 2004; Zhou et al. 1993). So we treat these sources as non cloud-cloud collision candidates.

We also check the galactic distributions for the four types of sources in Figure 6. The four types of sources are mostly located around the Galactic plane and the distributions are similar to the whole sample. This means the distributions toward the four types of sources are the same in our sample.

Figure 7 plots the kinematic distances of the four types of sources. The sources of type 1 are located in the first and second Galactic quadrants. Some type 1 sources are possibly associated with the Perseus arm. Type 2 and 3 sources are similar to the configuration of the distribution. Type 4 sources are just located around 5 kpc.

Figure 8 demonstrates the $L - V_{\rm LSR}$ diagram for the four types. The distributions for four types are roughly similar to the distribution of 201 sources. The last statistical data for the peak antenna temperature of the sources in the four types show some different distributions in Figure 9. The sources in type 1 show a bimodal distribution. From 2 K to 7 K, there is a large dispersion. The T_A^*
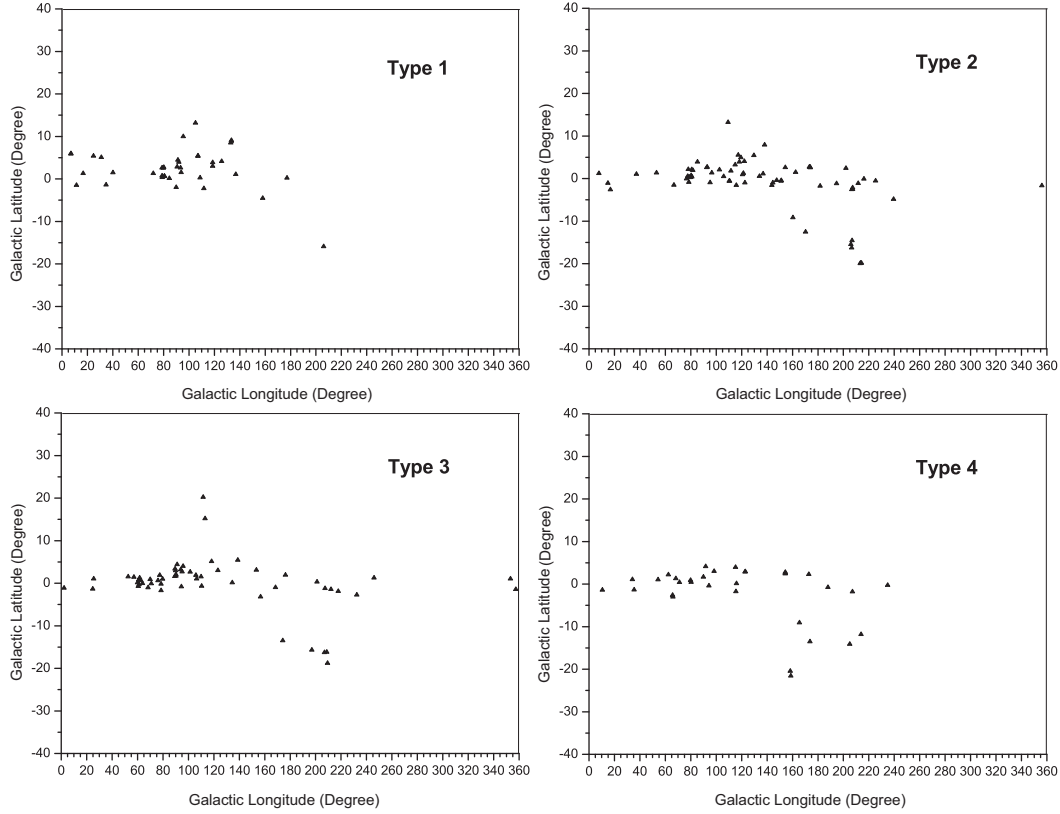
Fig. 6 Galactic distribution for four types of sources which are classified by the fit of the spectral profiles between the optically thick and thin lines.

range in type 2 is concentrated from 2 K to 5 K. The peak of the distribution in type 3 lies in 1–2 K. Type 4 shows a wide dispersion in the range 0–7 K.

Our next work will carry on mapping observations toward these possible cloud collision regions. We have recently selected some sources from our survey list to observe. We want to develop new methods to identify the cloud-cloud collision regions and get some new results of star formation triggered by cloud-cloud collisions.

4.3 Derived Parameters

Because of bad SNR in the ^{13}CO(1–0) line toward some sources in types 2, 3 and 4, we only calculate the parameters of the 38 sources in type 1. Derived parameters of the sources in type 1 have been listed in Table 3.

$T_{\mathrm{R}}^*(^{12}\mathrm{CO})$ and $T_{\mathrm{R}}^*(^{13}\mathrm{CO})$ are the ^{12}CO and ^{13}CO(1–0) radiation temperatures respectively; $T_{\mathrm{R}}^* = T_{\mathrm{A}}^*/\eta_{\mathrm{mb}}$, where T_{A}^* is the antenna temperature corrected with atmospheric attenuation and other losses (these are done by the observatory), and η_{mb} is the main beam efficiency. υ_{13} is the Gaussian fit of the $V_{\mathrm{LSR}}(^{13}\mathrm{CO})$ and $\Delta\upsilon_{13}$ is its full width at half-maximum (FWHM). The cores' distances from us are obtained from literatures (Wouterloot & Brand 1989). The ^{12}CO(1–0) line is usually considered to be optically thick in massive CO cores. Assuming local thermodynamic
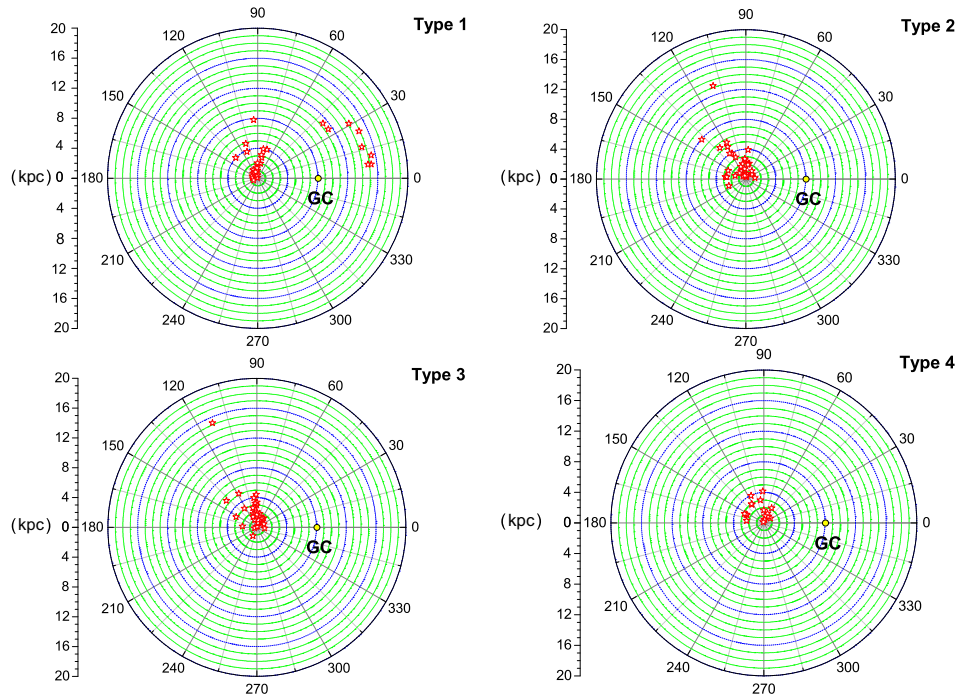
Fig. 7 Projected Galactocentric distribution toward four types of CO sources.
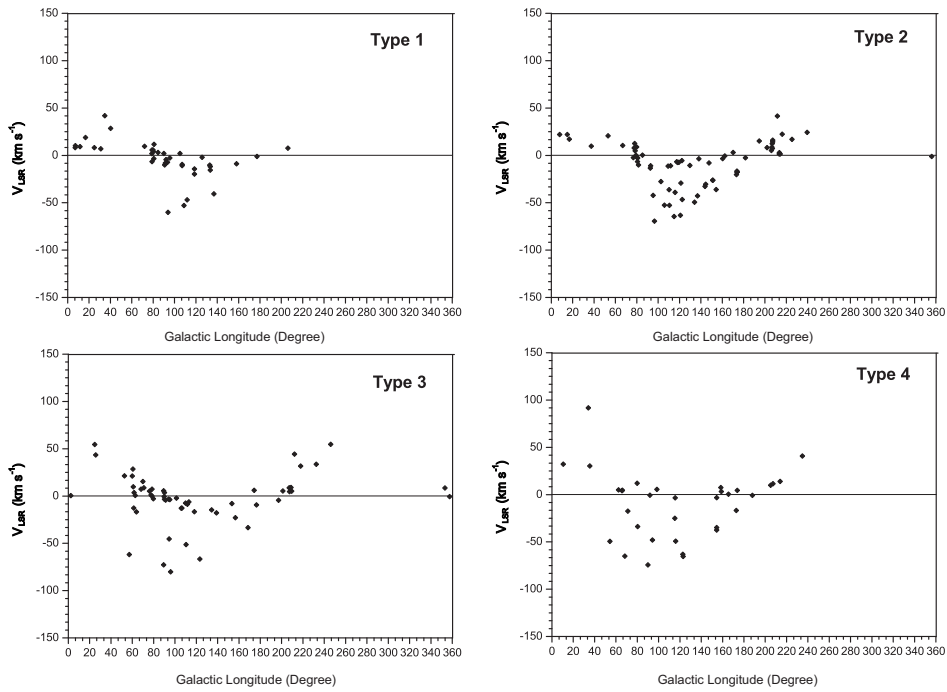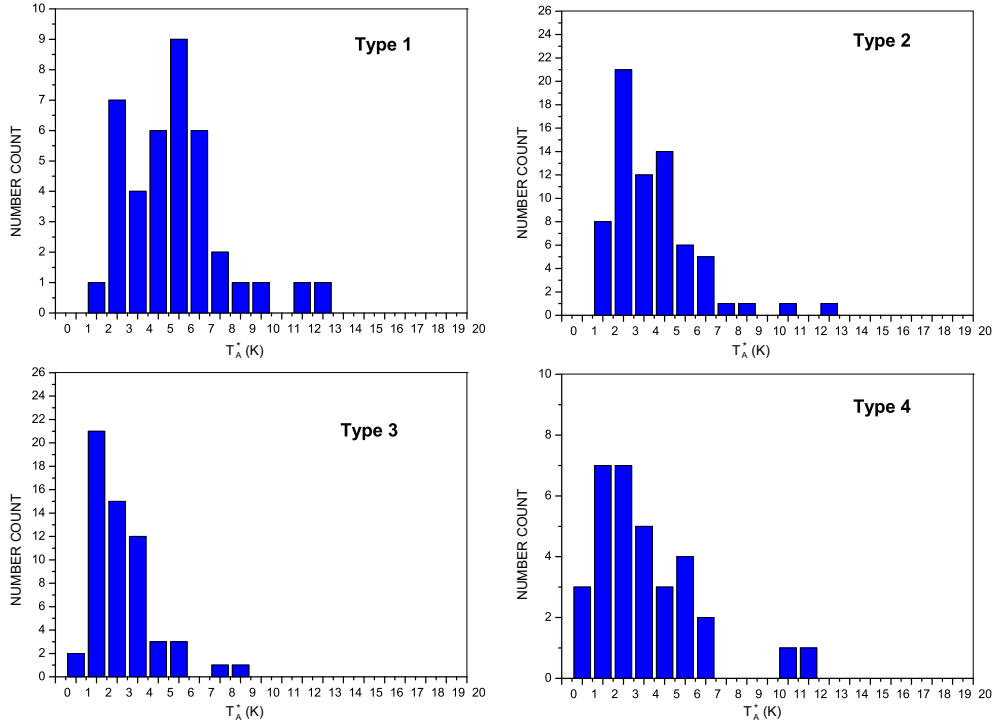

Fig. 8 L-V distribution for four types of sources in our survey sample.

Table 3 Parameters of the Sources in Type 1

IRAS	$T_R^*(^{12}CO)$ (K)	$T_R^*(^{13}CO)$ (K)	v_{13} (km s^{-1})	Δv_{13} (km s^{-1})	T_{ex} (K)	N_{H_2} (10^{22} cm^{-2})	τ_{13}
00056+6605	4.06	1.33	−6.24	0.91	8.47	0.17	0.40
	4.18	0.43	−2.58	1.65	8.59	0.05	0.11
00070+6516	8.54	5.06	−19.12	1.95	13.06	0.81	0.90
	3.15	1.22	−5.23	0.89	7.52	0.17	0.49
01166+6635	4.33	2.10	−2.51	0.93	8.75	0.30	0.66
	4.64	4.57	1.78	0.78	9.07	1.96	4.12
02425+6851	8.18	5.95	−10.83	1.57	12.69	1.12	1.30
	5.36	1.88	−4.08	0.77	9.81	0.23	0.43
02459+6029	13.07	9.54	−40.91	1.83	17.64	2.06	1.31
	18.22	5.57	−36.61	2.00	22.83	0.93	0.36
	3.40	1.61	−14.96	1.75	7.78	0.23	0.64
02485+6902	8.56	4.63	−10.57	1.94	13.08	0.71	0.78
	5.36	2.22	−3.59	0.62	9.81	0.29	0.54
	9.54	6.22	−15.57	3.05	14.07	1.09	1.06
02499+6911	6.35	1.61	−10.29	2.58	10.83	0.19	0.29
	5.55	3.10	−3.30	0.69	10.01	0.46	0.82
04173+4328	4.37	3.04	−8.61	0.85	8.79	0.53	1.19
05363+3127	5.19	3.14	−2.11	1.48	9.63	0.49	0.93
	9.17	5.14	1.20	1.23	13.69	0.81	0.82
05399−0121	10.66	2.65	2.52	2.33	15.21	0.34	0.29
	14.82	12.50	8.88	1.77	19.41	3.48	1.85
17364−1946	5.81	2.08	5.17	1.01	10.27	0.26	0.44
	4.87	6.69	10.50	1.64	9.31	. . .	. . .
17369−1945	4.52	2.81	5.27	0.81	8.95	0.45	0.97
	4.76	4.55	10.43	0.88	9.19	1.51	3.11
18134−1942	17.96	11.40	10.67	2.70	22.58	2.51	1.01
	7.75	5.61	21.49	1.08	12.25	1.04	1.29
18136−1347	11.50	4.55	19.36	2.08	16.06	6.65	0.50
	14.82	9.07	20.93	1.51	19.41	1.78	0.95
18273+0034	5.52	5.50	8.08	1.80	9.97	3.46	6.19
	4.68	5.97	9.93	1.46	9.11	. . .	. . .
18567+0700	17.75	11.27	29.20	2.63	22.36	2.47	1.01
	5.96	1.39	32.97	2.64	10.43	0.16	0.26
18572+0057	6.02	2.39	37.53	2.84	10.49	0.31	0.50
	8.66	5.18	45.68	4.51	13.18	0.84	0.91
20051+3435	9.48	5.59	11.11	3.25	14.01	0.92	0.89
20190+4102	16.27	8.77	2.84	1.35	20.88	1.67	0.77
20227+4154	12.86	11.19	5.58	2.23	17.43	3.14	2.04
	5.65	1.24	10.48	2.42	10.11	0.14	0.25
20228+4215	23.44	15.47	5.50	1.68	28.08	4.08	1.08
	5.96	1.28	8.00	4.71	10.43	0.15	0.24
20275+4001	14.80	9.28	−5.81	3.41	19.39	1.85	0.99
	5.75	2.32	0.45	1.87	10.21	0.30	0.52
20293+3952	10.91	9.54	5.78	3.04	15.47	2.56	2.07
20332+4124	15.32	9.66	−2.02	3.39	19.92	1.96	1.00
	5.46	1.92	4.57	1.92	9.91	0.24	0.43
20343+4129	3.24	1.24	−2.72	1.58	7.62	0.17	0.48
	11.69	4.42	11.62	2.48	16.25	0.64	0.48
20436+5849	5.77	3.16	−2.29	1.39	10.23	0.47	0.79
	4.35	0.96	3.60	1.13	8.77	0.11	0.25
20489+4410	17.89	10.80	−2.16	2.20	22.50	2.30	0.93
	10.18	1.92	2.47	4.77	14.72	0.24	0.21
20553+5208	7.09	5.48	−8.46	2.01	11.58	1.08	1.49
	5.34	1.81	−3.21	2.31	9.79	0.23	0.42
21005+5217	4.08	1.26	−10.77	1.70	8.49	0.16	0.37
	5.22	3.53	−1.54	3.67	9.67	0.60	1.12
21007+5036	10.64	7.44	−10.33	1.91	15.19	1.43	1.20
	3.61	0.96	−1.83	4.90	8.00	0.12	0.31

Table 3 —*Continued.*

IRAS	$T_R^*(^{12}CO)$ (K)	$T_R^*(^{13}CO)$ (K)	v_{13} (km s^{-1})	Δv_{13} (km s^{-1})	T_{ex} (K)	N_{H_2} (10^{22} cm^{-2})	τ_{13}
21131+5221	4.89	3.10	−13.49	1.57	9.33	0.50	1.00
	8.10	5.81	−5.73	3.67	12.61	1.07	1.26
21169+6804	5.50	5.48	3.02	0.97	9.95	3.40	6.10
21182+4641	11.01	9.28	1.62	1.25	15.56	2.31	1.85
	4.51	0.82	5.57	1.16	8.93	0.09	0.20
21202+5157	13.34	3.63	−59.20	2.39	17.92	0.51	0.32
	2.64	0.90	−54.12	1.17	6.99	0.13	0.41
22199+6322	16.41	9.42	−10.64	1.70	21.01	1.86	0.85
	8.16	2.69	−7.05	1.09	12.67	0.34	0.40
22202+6317	11.56	4.69	−10.88	1.40	16.11	0.69	0.52
	6.35	4.08	−7.36	1.56	10.83	0.67	1.03
22528+5936	14.08	7.46	−53.25	2.05	18.66	1.32	0.75
23215+5826	9.63	3.04	−46.59	1.44	14.17	0.40	0.38

Fig. 9 Statistical distribution of T_A^* for four types of sources in our survey sample.

equilibrium (LTE), the excitation temperature T_{ex} of the ^{13}CO(1–0) transition is the same as that of ^{12}CO (Garden et al. 1991).

$$T_{ex} = \frac{h\nu}{k} \left\{ \ln\left[1 + \left(\frac{kT_R^*(^{12}CO)}{h\nu} + \frac{1}{\exp\left(\frac{h\nu}{kT_{bg}} - 1\right)}\right)^{-1}\right]\right\}^{-1}, \qquad (1)$$

where $T_{\mathrm{bg}} = 2.7\,\mathrm{K}$. The ^{13}CO(1–0) transition is usually optically thin. On the LTE assumption, the opacity of ^{13}CO(1–0) is approximately (Guan et al. 2008)

$$\tau(^{13}\mathrm{CO}) \approx -\ln\left[1 - \frac{T_{\mathrm{R}}^*(^{13}\mathrm{CO})}{T_{\mathrm{R}}^*(^{12}\mathrm{CO})}\right].$$ (2)

Sometimes the ^{12}CO spectra are self-reversed by absorption from the cold part of the cloud's outer core. In that case, the opacity of ^{13}CO will be underestimated. The ^{13}CO column density is given by (Garden et al. 1991)

$$N(^{13}\mathrm{CO}) = \frac{3k}{8\pi^3 B\mu^2} \frac{\exp\left[\frac{hBJ(J+1)}{kT_{\mathrm{ex}}}\right]}{J+1} \times \frac{T_{\mathrm{ex}} + hB/3k}{[1 - \exp(\frac{-h\nu}{kT_{\mathrm{ex}}})]} \int \tau_\nu \, d\nu.$$ (3)

Here B is the rotational constant of ^{13}CO, μ is the permanent dipole moment and J is the rotational quantum number of the lower state.

We adopt the ^{12}CO and ^{13}CO abundances to be

$$\frac{N(\mathrm{H_2})}{N(^{12}\mathrm{CO})} = 10000, \quad \frac{N(^{12}\mathrm{CO})}{N(^{13}\mathrm{CO})} = 89.$$ (4)

4.4 Infrared Results

We draw the color cuts used for the IRAS sources in our survey for cloud-cloud collision candidates. The color cuts used here were derived from values in the literature and were taken from studies of several types of objects: T Tauri stars, low-mass and intermediate-mass YSOs, and massive YSOs.

Table 4 lists the color cuts we used. We use the criteria to select the YSO candidates, but it is not a unique classification method. The choice of color cuts is merely meant to be as inclusive as possible. All the results plotted in the color-color diagram are represented in Figure 10. The sources of the three types which are considered as possible cloud-cloud collision candidates are marked on the map.

Table 4 *IRAS* Color Cuts Used For Selection Of YSOs

Object Type	[25–12]	[60–25]	[100–60]	Reference
T Tauri stars	0–0.6	<0.5	…	[1, 2]
Intermediate-mass YSOs	0–1.0	0.4–1.0	…	[3]
High-mass YSOs	0.17–1.5	0.23–1.13	0.08–0.57	[4]

Notes: $[\lambda1 - \lambda2] = \log(F1/F2)$. [1] Harris et al. (1988); [2] Prusti et al. (1992); [3] Beichman et al. (1986); [4] Bronfman et al. (1996).

According to the range of the IRAS cuts given by Table 4, we summarize that three T Tauri stars, 25 intermediate-mass YSOs and 24 high-mass YSOs are identified from the type 1 sources. There are two T Tauri stars, 30 intermediate-mass YSOs and 22 high-mass YSOs identified in type 2. In type 3, 23 intermediate-mass YSOs and 27 high-mass YSOs are identified from the 58 sources but there are no T Tauri stars.

5 CONCLUSIONS

In this paper, according to the criteria for a cloud-cloud collision sample, we observed the ^{12}CO, ^{13}CO and C^{18}O(J=1–0) lines in 201 *IRAS* sources which were selected as cloud-cloud collision candidates. The criteria are as follows:
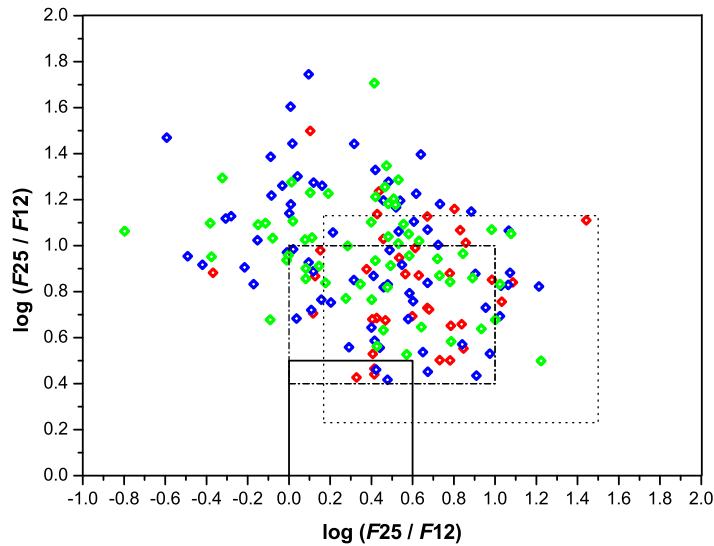
Fig. 10 The color-color distribution of the sources in types 1, 2 and 3. The red, blue and green diamonds represent the sources in types 1, 2 and 3, respectively. The color box of T Tauri stars is indicated by the solid line. The dash-dotted box covers the intermediate-mass YSOs and the dotted box shows the location of the high-mass YSOs.

(1) A set of criteria given by Vallee (1995b) which describe the spectral properties of the possible cloud-cloud collision region.
(2) The line profile features show the feature of a double or multiple peak and the velocity of peaks are adjacent.

These sources are located over a wide range of Galactocentric distances, and partly associated with the star formation region. Then the 201 sources are classified into four types by the close fit between the profile of optically thick ^{12}CO lines and those of the optically thin ^{13}CO and C^{18}O. The *IRAS* flux in four bands has been used to identify sources whose colors are similar to those of YSOs. Considering the association of the *IRAS* and *MSX* PSC, the sources in types 1, 2 and 3 could be selected to do the multi-wavelength mapping, to see if there is star formation triggered by cloud-cloud collision. Toward two possible cloud-cloud collision candidates (*IRAS* 02459+6029 and 22528+5936) selected from our survey, combining the CO mapping and multi-wavelength study we demonstrate that *IRAS* 02459+6029 could be a cloud-cloud collision sample and *IRAS* 22528+5936 could be two separate clouds that are not colliding (Li & Wang 2012). We also develop our new criteria to identify the cloud-cloud collision region in that paper. This survey is very foundational and efficient for selecting possible cloud-cloud collision regions.

References

Beichman, C. A. 1986, in Light on Dark Matter, Astrophysics and Space Science Library, 124, ed. F. P. Israel (Dordrecht: Reidel), 279
Beichman, C. A., Myers, P. C., Emerson, J. P., et al. 1986, ApJ, 307, 337
Bronfman, L., Nyman, L.-A., & May, J. 1996, A&AS, 115, 81
Dobashi, K., Onishi, T., Iwata, T., et al. 1993, AJ, 105, 1487

Frerking, M. A., & Langer, W. D. 1982, ApJ, 256, 523

Garden, R. P., Hayashi, M., Hasegawa, T., Gatley, I., & Kaifu, N. 1991, ApJ, 374, 540

Gilden, D. L. 1984, ApJ, 279, 335

Goldreich, P., & Kwan, J. 1974, ApJ, 189, 441

Guan, X., Wu, Y., & Ju, B. 2008, MNRAS, 391, 869

Habe, A., & Ohta, K. 1992, PASJ, 44, 203

Harris, S., Clegg, P., & Hughes, J. 1988, MNRAS, 235, 441

Hausman, M. A. 1981, ApJ, 245, 72

Kerton, C. R., & Brunt, C. M. 2003, A&A, 399, 1083

Lattanzio, J. C., Monaghan, J. J., Pongracic, H., & Schwarz, M. P. 1985, MNRAS, 215, 125

Li, N., & Wang, J. J. 2012, RAA (Research in Astronomy and Astrophysics), 12, 1269

Prusti, T., Adorf, H.-M., & Meurs, E. J. A. 1992, A&A, 261, 685

Vallee, J. P. 1995a, AJ, 109, 1724

Vallee, J. P. 1995b, AJ, 110, 2256

Walsh, W., Beck, R., Thuma, G., et al. 2002, A&A, 388, 7

Wang, J.-J., Chen, W.-P., Miller, M., Qin, S.-L., & Wu, Y.-F. 2004, ApJ, 614, L105

Wouterloot, J. G. A., & Brand, J. 1989, A&AS, 80, 149

Xin, B., & Wang, J.-J. 2008, ChJAA (Chin. J. Astron. Astrophys.), 8, 433

Yang, J., Jiang, Z., Wang, M., Ju, B., & Wang, H. 2002, ApJS, 141, 157

Zhou, S., Evans, N. J., II, Koempe, C., & Walmsley, C. M. 1993, ApJ, 404, 232